

# Quantum Monte Carlo calculations of two neutrons in finite volume

P. Klos,<sup>1,2,\*</sup> J. E. Lynn,<sup>1,2</sup> I. Tews,<sup>3</sup> S. Gandolfi,<sup>4</sup> A. Gezerlis,<sup>5</sup> H.-W. Hammer,<sup>1,2</sup> M. Hoferichter,<sup>3</sup> and A. Schwenk<sup>1,2</sup>

<sup>1</sup>*Institut für Kernphysik, Technische Universität Darmstadt, 64289 Darmstadt, Germany*

<sup>2</sup>*ExtreMe Matter Institute EMMI, GSI Helmholtzzentrum für Schwerionenforschung GmbH, 64291 Darmstadt, Germany*

<sup>3</sup>*Institute for Nuclear Theory, University of Washington, Seattle, WA 98195-1550, USA*

<sup>4</sup>*Theoretical Division, Los Alamos National Laboratory, Los Alamos, NM 87545, USA*

<sup>5</sup>*Department of Physics, University of Guelph, Guelph, Ontario N1G 2W1, Canada*

*Ab initio* calculations provide direct access to the properties of pure neutron systems that are challenging to study experimentally. In addition to their importance for fundamental physics, their properties are required as input for effective field theories of the strong interaction. In this work, we perform auxiliary-field diffusion Monte Carlo calculations of the ground and first excited state of two neutrons in a finite box, considering a simple contact potential as well as chiral effective field theory interactions. We compare the results against exact diagonalizations and present a detailed analysis of the finite-volume effects, whose understanding is crucial for determining observables from the calculated energies. Using the Lüscher formula, we extract the low-energy  $S$ -wave scattering parameters from ground- and excited-state energies for different box sizes.

## I. INTRODUCTION

A major challenge of nuclear physics is the direct calculation of nuclear observables from the underlying theory of quantum chromodynamics (QCD). The most promising strategy today towards this goal involves lattice QCD calculations for small nuclei and a sequence of matching steps to advanced few- and many-body methods based on effective field theories (EFTs) for nuclear forces.

Solving QCD on a lattice of discretized spacetime in Euclidean space represents the only method to calculate nuclear observables from the QCD Lagrangian [1]. Numerical calculations are only feasible in a finite box where the energy spectrum is discrete. Below the first inelastic threshold, Lüscher [2, 3] established a direct connection between the scattering phase shifts in the infinite volume and finite-volume energy levels for two-particle scattering. The extension of this connection to the three-particle sector is the subject of ongoing research (see, for example, Refs. [4–7]). As a consequence, the scattering parameters, such as the scattering length and effective range, can be extracted from finite-volume energy levels obtained from lattice QCD. However, as the Lüscher result corresponds to an EFT in which particles interact only via contact interactions [8], it is not applicable to the regime of nuclear physics where the nonanalyticities from pion exchange become important, i.e., where exponential corrections start to set in.

Chiral EFT offers a framework to include explicit pions into the EFT for low-energy nucleons [9, 10]. It has been very successful in the past years and is used extensively to calculate the properties of nuclei, electroweak transitions, and matter under extreme conditions [11–16]. Chiral EFT is based on the chiral symmetry of QCD and provides a systematic framework for nuclear forces; in particular it predicts a hierarchy between two- and

multi-nucleon forces as well as external currents. It is therefore possible to obtain a generalization of Lüscher’s result that includes pions by matching finite-volume results from chiral EFT interactions to lattice QCD calculations. This matching to chiral EFT is done through adjustment of so-called low-energy constants (LECs), which incorporate the degrees of freedom that were integrated out. Once the LECs are determined, one is able to calculate phase shifts in the infinite volume using few- and many-body methods to solve the Schrödinger equation. In this way, scattering parameters in the infinite volume can be obtained also from finite-volume calculations in smaller boxes where pion exchanges become relevant.

Presently, the LECs in chiral EFT are fit to experimental data, a strategy that fails in channels where experimental data are scarce or even nonexistent, such as the three-neutron system. A future alternative strategy consists of applying LECs matched to lattice QCD to calculate other observables, which would provide a fully QCD-based prediction for these observables. At present, lattice QCD calculations for systems with more than one nucleon are only available for nonphysical quark masses. However, if the quark masses are within the range of applicability of the chiral expansion, chiral EFT also allows one to extrapolate to physical values and, in the process, determine the LECs that govern the quark mass dependence, which are largely unknown to date.

In this work, we perform finite-volume calculations of two particles with chiral EFT interactions matched to experimental data. We focus on the neutron-neutron ( $nn$ ) system, motivated also by the fact that the corresponding scattering length cannot be measured directly and controversial data from indirect measurements would make an independent *ab initio* verification particularly valuable [17]. Our long-term goal is to establish a technique to match chiral nuclear interactions to data from lattice QCD. This would allow the extraction of the LECs which appear in chiral EFT directly from the lattice and thus facilitate a path to calculate nuclear observables of larger nuclei directly from QCD. To set the foundation

---

\* E-mail: pklos@theorie.ikp.physik.tu-darmstadt.de

for future work towards matching two- and higher-body systems, we require a numerical method that is easily scalable to many particles and is well suited to studies in periodic boundary conditions. We use the auxiliary-field diffusion Monte Carlo (AFDMC) method, since it represents a very accurate method (see, for example, Refs. [18, 19] for recent reviews), for which calculations with chiral EFT interactions have become possible only recently [20–24]. Furthermore, performing finite-volume calculations is straightforward in Quantum Monte Carlo (QMC) as coordinate space is intrinsically constrained. A similar study on how to exploit input from lattice QCD for determining LECs in pionless EFT using AFDMC calculations can be found in Refs. [25, 26].

In this paper, we benchmark QMC calculations in finite volume for ground and excited states, both for a contact potential as well as chiral EFT interactions. In particular, we verify that QMC finite-volume calculations, by means of the Lüscher formalism, reproduce the low-energy effective-range parameters corresponding to a given  $nn$  potential. We thereby demonstrate that such QMC calculations provide a reliable tool to establish a bridge between lattice QCD calculations and chiral EFT, in particular in kinematic configurations where the consideration of pion exchanges becomes mandatory and the Lüscher formula cannot be applied straightforwardly.

Generalizations of the Lüscher formalism to multi-body systems prove to be fairly complex [4–7], to the point that alternative strategies to extract infinite-volume physics from finite-volume energy levels might be welcome. For QMC methods to contribute in this direction, especially for channels where resonances may occur, it is crucial that excited states can also be accessed, in order to be able to identify the expected avoided level crossing [27, 28]. This presents a challenge. Quantum Monte Carlo methods were developed to solve the many-body Schrödinger equation of a given system and find the lowest-energy state. As this particular state is given by the bosonic solution, nodal surfaces in the many-body wave function have to be introduced, something which can only be done approximately [18, 29, 30]. While an exact solution to this problem is therefore not available at the moment, we propose a strategy to obtain an approximate numerical solution for the excited state. Although the  $nn$  system strictly speaking does not exhibit a resonance, but only a virtual state, the  $nn$  calculations presented in this paper can be considered a first step towards this application.

This paper is organized as follows. A brief summary of the Lüscher formula is presented in Sec. II. Section III gives an overview of the AFDMC method for ground and excited states. A special emphasis is placed on the construction of trial wave functions that become important for the calculation of excited states. In Sec. IV, we present AFDMC results for finite-volume calculations of  $nn$  energies for a contact potential as well as chiral EFT interactions at different orders. Both ground states and excited states are compared with results from the Lüscher

formula and also to exact diagonalizations. Based on this, we analyze in detail the finite-volume effects and deviations caused by pion exchanges. We then successfully extract scattering parameters from the finite-volume results using the Lüscher formula. Finally, we conclude in Sec. V.

## II. LÜSCHER FORMULA

The very low-momentum properties of nucleon-nucleon (NN) interactions can be efficiently described within a pionless EFT [31–33]. Constrained to short-range interactions the Lagrangian becomes a series of local operators that consist of derivatives acting on nucleon fields. Applying dimensional regularization with power-divergence subtraction [31], the scattering amplitude for two-body elastic scattering can be written in terms of a single scalar integral, whose divergent part becomes absorbed into the renormalization of the LECs of the theory. In a box of size  $L^3$  with periodic boundary conditions it is then possible to relate the energy eigenstates of the two-body system to the  $S$ -wave phase shift  $\delta_0(p)$  in infinite volume. The eigenvalues for the energy  $E = p^2/M$ , with relative momentum  $p$  and nucleon mass  $M$ , are given in terms of solutions of the Lüscher formula [2, 3]<sup>1</sup>

$$p \cot \delta_0(p) = \frac{1}{\pi L} S \left( \left( \frac{Lp}{2\pi} \right)^2 \right). \quad (1)$$

$S(\eta)$  can be defined as a regulated sum

$$S(\eta) = \lim_{\Lambda \rightarrow \infty} \left( \sum_{|\mathbf{j}| < \Lambda} \frac{1}{\mathbf{j}^2 - \eta} - 4\pi\Lambda \right), \quad (2)$$

which runs over all three-vectors of integers  $\mathbf{j}$  with  $|\mathbf{j}| < \Lambda$ . A more detailed discussion of  $S(\eta)$  as well as its practical implementation for a numerical evaluation are summarized in Appendix A.

This form of the Lüscher formula emerges naturally in pionless EFT when the loop integral is replaced by a discrete sum over the momentum states allowed on the lattice [8]. In this derivation, Eq. (1) strictly holds as long as a description in pionless EFT is justified. Due to the  $t$ -channel cut in the one-pion exchange, this restricts its range of validity to  $|p| < m_\pi/2$  in the complex  $p$  plane. However, as shown in Refs. [2, 3], corrections to Eq. (1) for momenta below the first inelastic threshold  $|p| < \sqrt{m_\pi M}$  are suppressed by  $e^{-m_\pi L}$ , so that in practice the relation can be used as long as  $m_\pi L$  is sufficiently large. In Ref. [34], the size of these corrections in

<sup>1</sup> This version only holds for an  $S$ -wave projected potential, with corrections entering at the level of  $G$ -waves. We considered the corresponding generalized relation [2, 3] as well, but found the corrections to be negligible due to the large suppression of the physical  $G$ -wave phase shift.

the two-nucleon system was estimated for EFT-inspired potentials with pion exchange and contact interactions.

For low-energy  $NN$  scattering the first parameters of the effective-range expansion, the scattering length  $a$  and the effective range  $r_e$ , are sufficient for an accurate description of the phase shift:

$$p \cot \delta_0(p) = -\frac{1}{a} + \frac{1}{2}r_e p^2 + \mathcal{O}(p^4). \quad (3)$$

Therefore, it is possible for a given scattering length and effective range to predict the energies of ground and excited states in a finite volume. Vice versa, given a set of data points  $\{E_i, \Delta E_i\}$  for the energy eigenvalues for different box sizes  $L_i$  one can determine the scattering parameters  $a$  and  $r_e$  that best fulfill Eq. (1), where the left-hand side has been replaced by Eq. (3). In fact, whenever energy levels become negative, Eq. (1) provides a constraint in the unphysical region that cannot immediately be translated into a corresponding value for the phase shift. In such cases, the effective-range expansion (3), in addition to providing a convenient parametrization of the phase shift, serves another purpose, namely that of stabilizing the analytic continuation towards the physical region, which can only be performed if the functional form is known. This situation is realized for the ground-state energy of the two-neutron system.

Although Eq. (1) could still be used for  $m_\pi/2 < |p| < \sqrt{m_\pi M}$  provided the volume is sufficiently large, the validity of the analytic continuation based on the effective-range expansion (3) is limited by the  $t$ -channel pion exchange, which in the partial-wave projection generates cuts on the imaginary momentum axis starting at  $p = \pm i m_\pi/2$ . Therefore, if points with  $|p| > m_\pi/2$  were to be included, these cuts would have to be accounted for explicitly in the functional form used in the analytic continuation. For this reason we restrict all fits in this paper to points within the strict radius of convergence of pionless EFT  $|p| < m_\pi/2$ .

Since  $S(\eta)$  is not invertible, it is not possible to directly define a function  $E = E(L, a, r_e)$  which could be used in a standard  $\chi^2$  fit, so that we minimize instead

$$\chi^2 = \sum_{i=1}^N \frac{\left( \frac{1}{a} - \frac{1}{2}r_e M E_i + \frac{1}{\pi L_i} S\left(\left(\frac{L_i}{2\pi}\right)^2 M E_i\right) \right)^2}{\sigma_i^2}, \quad (4)$$

with standard deviations obtained from Gaussian error propagation

$$\sigma_i^2 = \left[ -\frac{1}{2}r_e M + \frac{M L_i}{4\pi^3} S'\left(\left(\frac{L_i}{2\pi}\right)^2 M E_i\right) \right]^2 (\Delta E_i)^2, \quad (5)$$

and  $S'(\eta) = dS(\eta)/d\eta$ . Parameter errors are estimated from the Hessian

$$H = \frac{1}{2} \left( \begin{array}{cc} \frac{\partial^2 \chi^2}{\partial a^2} & \frac{\partial^2 \chi^2}{\partial a \partial r_e} \\ \frac{\partial^2 \chi^2}{\partial r_e \partial a} & \frac{\partial^2 \chi^2}{\partial r_e^2} \end{array} \right) \Big|_{a_{\min}, (r_e)_{\min}}, \quad (6)$$

according to

$$\Delta a = \sqrt{(H^{-1})_{11}}, \quad \Delta r_e = \sqrt{(H^{-1})_{22}}. \quad (7)$$

Based on these equations we demonstrate the feasibility of an extraction of scattering parameters from finite-volume QMC calculations in Sec. IV, for both a contact potential as well as chiral EFT interactions.

### III. QUANTUM MONTE CARLO

The AFDMC method has been successfully applied to both homogeneous and inhomogeneous neutron matter in the past decade (see Refs. [18, 19] for a summary of results and a more detailed description of the method) and more recently has shown promising progress towards generalization to nuclear matter and nuclei [35]. In this section we review the basic concepts of the AFDMC method and how it was applied in the two-neutron system. We give particular attention to the calculation of excited states, which is in general a nontrivial task for QMC methods.

The aim of diffusion Monte Carlo methods is to solve the many-body Schrödinger equation by means of stochastically projecting out the lowest-energy state from a given trial wave function  $\psi_T$ ,

$$\psi(\tau) = e^{-(H-E_T)\tau} \psi_T, \quad (8)$$

where the trial energy  $E_T$  is a constant that is used to control the normalization. In the limit of large imaginary time  $\tau = it$ , only the lowest-energy state not orthogonal to  $\psi_T$  survives:  $\psi(\tau \rightarrow \infty) \rightarrow \psi_0$ . Therefore, the choice of a trial wave function with symmetries appropriate to the state under study is an important consideration, a point to which we return when discussing the calculation of excited states. For strongly interacting many-body systems it is not possible to calculate directly the imaginary-time propagator

$$G_{\alpha\beta}(\mathbf{R}, \mathbf{R}'; \tau) = \langle \alpha, \mathbf{R} | e^{-(H-E_T)\tau} | \beta, \mathbf{R}' \rangle, \quad (9)$$

where  $\mathbf{R} = \{\mathbf{r}_1, \mathbf{r}_2, \dots, \mathbf{r}_A\}$  is the configuration vector of the  $A$  nucleons and  $\alpha, \beta$  are spin-isospin indices. However, in the small imaginary-time limit, the calculation is tractable and the propagation is performed as a sequence of small-time evolutions. Then, the realization of Eq. (8) is given by the path integral (omitting the spin-isospin labels)

$$\psi(\mathbf{R}_N, \tau) = \int \prod_{i=0}^{N-1} d\mathbf{R}_i G(\mathbf{R}_{i+1}, \mathbf{R}_i; \Delta\tau) \psi_T(\mathbf{R}_0), \quad (10)$$

where  $\Delta\tau$  is the small imaginary time step and the paths  $\mathbf{R}_i$  are sampled by Monte Carlo.

The AFDMC method takes as a basis state the tensor product of the  $3A$  coordinates of the  $A$  nucleons and the

tensor product of the four complex amplitudes for each nucleon to be in a state  $|s\rangle = |p \uparrow, p \downarrow, n \uparrow, n \downarrow\rangle$ . That is,

$$|\mathbf{R}S\rangle = |\mathbf{r}_1 s_1\rangle \otimes |\mathbf{r}_2 s_2\rangle \otimes \cdots \otimes |\mathbf{r}_{ASA}\rangle. \quad (11)$$

As a consequence of the choice of basis, the propagator must contain, at most, linear operators in spin-isospin space. Therefore, the Hubbard-Stratonovich transformation is used to linearize quadratic operators in the Hamiltonian

$$e^{O^2/2} = \frac{1}{\sqrt{2\pi}} \int_{-\infty}^{\infty} dx e^{-x^2/2} e^{xO}, \quad (12)$$

introducing the auxiliary fields  $x$ , which are Monte Carlo sampled to perform the integrals. This choice provides for polynomial scaling with nucleon number, because the spin-isospin states are sampled instead of summed explicitly as in, for example, the Green's function Monte Carlo (GFMC) method [18].

In this work, we take a Jastrow trial wave function, which is a product of central correlations acting on a Slater determinant of single-particle orbitals,

$$|\psi_J\rangle = \left[ \prod_{i<j} f^c(r_{ij}) \right] |\Phi\rangle, \quad (13)$$

with  $\langle \mathbf{R}S|\Phi\rangle = \mathcal{A}[\langle \mathbf{r}_1 s_1|\phi_1\rangle \cdots \langle \mathbf{r}_2 s_2|\phi_2\rangle \cdots \langle \mathbf{r}_{ASA}|\phi_A\rangle]$ . The Jastrow wave function incorporates the dominant short-range central correlations into the wave function, by a solution of the radial Schrödinger equation in the given spin-isospin channel of the Hamiltonian. For neutrons in a cubic periodic box of volume  $L^3$ , the single-particle orbitals are taken as plane waves:  $\phi_\alpha(\mathbf{r}_i, s_i) = e^{i\mathbf{k}_\alpha \cdot \mathbf{r}_i} \chi_{s, m_s}(s_i)$ , with  $\mathbf{k}_\alpha = \frac{2\pi}{L} \mathbf{n}_\alpha$  and  $\mathbf{n}_\alpha$  being a vector of integers.  $\chi_{s, m_s}$  denotes the spin eigenstates. For two neutrons, only the lowest two states with  $\mathbf{k}_1 = \mathbf{k}_2 = \mathbf{0}$  are occupied, leaving the Slater determinant  $\langle \mathbf{R}S|\Phi\rangle$  independent of spatial coordinates.

Imposing periodic boundary conditions is equivalent to identifying the endpoints of each Cartesian interval. This implies that, in coordinate space, the potential includes, in addition to the original potential  $V(\mathbf{r})$ , copies from the surrounding boxes

$$V(\mathbf{r}) \rightarrow \sum_{\mathbf{n} \in \mathbb{Z}^3} V(\mathbf{r} + \mathbf{n}L) \quad (14)$$

to preserve periodicity [2]. As long as the range of the potential, characterized by the effective range  $r_e$  for example, is small compared to the box size,  $r_e \ll L$ , the higher terms in the sum in Eq. (14) can be safely ignored. However, when the box size becomes comparable to the range of the potential  $L \sim r_e$ , these higher terms need to be included in both the expectation value of the Hamiltonian and in the calculation of the propagator in order to maintain the periodic boundary conditions. Below, if necessary, we consider terms corresponding up to either the nearest, second-to-nearest, or third-to-nearest boxes

around the original one and thereby check for convergence of the sum in Eq. (14).

The calculation of excited states can be a challenging task for diffusion Monte Carlo methods. Since such methods always project, out of a trial wave function, the lowest-energy state of a given Hamiltonian, care must be taken to ensure orthogonality to, for example, the ground state (if the first-excited-state solution is sought). For nuclei, in many cases, the excited state which is desired has quantum numbers distinct from the ground state. In this case, all that is required is to construct a trial wave function with the appropriate quantum numbers [36]. However, in some cases, for example the Hoyle state of  $^{12}\text{C}$ , the desired excited state has the same quantum numbers as the ground state, and then more care in constructing an appropriate trial wave function is required [30]. In the two-neutron system for low-energy scattering, we consider only the case where the neutrons are in a singlet spin state ( $^1S_0$ ), which corresponds to the state described by the Lüscher formula in Sec. II, and therefore the excited states possess the same quantum numbers as the ground state. Such excited scattering states have not been calculated previously using the AFDMC method.

The trial wave function for the first excited state calculated here was determined as follows. We assume a nodal surface defined by a particular relative distance  $r_{\text{node}}$  between the two particles. Since our Slater determinant is spatially independent, we introduce the node in the central correlation of the Jastrow wave function such that  $\psi_J(r_{\text{node}}) = 0$ . This implies that there is no angular dependence and the nodal surface is a sphere in relative coordinates. The validity of this assumption and an estimate for the related systematic error as well as an improved nodal surface will be discussed later. To determine the nodal position, we adopt the iterative approach described below.

Quantum Monte Carlo methods typically require local potentials. For an eigenstate of a local Hamiltonian, the solution of the Schrödinger equation must yield the same energy independent of the coordinates at which it is evaluated. Evaluating  $[H\psi(\mathbf{R})]/\psi(\mathbf{R})$ , where  $\psi$  is the exact solution of the problem, should therefore yield the same energy for a configuration of the two particles  $\mathbf{R} = \{\mathbf{r}_1, \mathbf{r}_2\}$  with relative distance  $r < r_{\text{node}}$  or  $r > r_{\text{node}}$ . As a consequence, the node position can be obtained by performing separate AFDMC simulations in the two subspaces divided by the nodal surface and adjusting the node position such that the AFDMC energies in the two subspaces agree. Each of these simulations starts from initial configurations where all walkers are placed in one of the two subspaces. For an arbitrarily chosen node position the two simulations will yield different energies. Moving the node position in the relative coordinate such that the two independent simulations yield the same energy within statistical uncertainties leads to the results presented in the next section. As the constrained-path approximation [37], which we use to tame the sign problem, prohibits walkers from crossing the nodal sur-

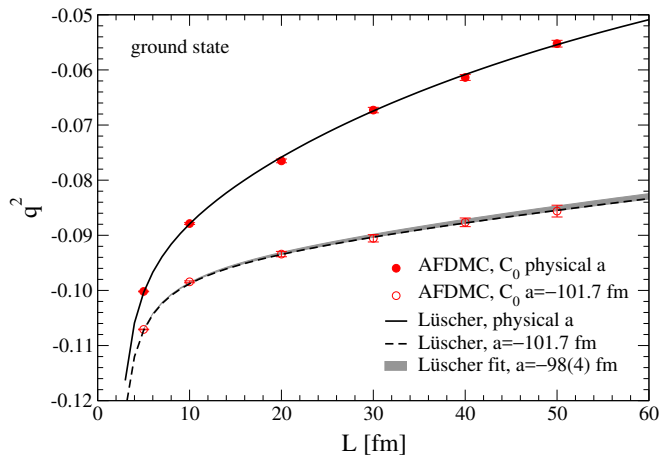


FIG. 1. (Color online) AFDMC results for the energy of two neutrons in the ground state in finite volume with the contact potential (15) for different box sizes  $L$  compared with the Lüscher formula.  $C_0$  is adjusted to give the physical  $nn$  scattering length  $a = -18.9$  fm (closed circles and solid line) and to give a very large scattering length  $a = -101.7$  fm (open circles and dashed line). The gray band shows a fit (as described in the text) to the AFDMC results for  $a = -101.7$  fm. The energies are given in terms of the dimensionless quantity  $q^2 = EML^2/(4\pi^2)$ .

face, this is equivalent to performing a simulation in a space which is limited to the region where the trial wave function does not change sign.

#### IV. RESULTS

We perform AFDMC simulations of two neutrons in a cubic box with periodic boundary conditions for both a simple contact potential as well as chiral EFT interactions. Both ground-state and first-excited-state energies are calculated and compared to exact solutions derived from the Lüscher formula in Eq. (1) with the effective range expansion in Eq. (3). The box size was varied from  $L = 5$  fm to  $L = 50$  fm.

##### A. Contact interaction

First, we consider a contact interaction independent of spin and isospin operators smeared out by a regulating function  $V(r) = C_0\delta(r) \rightarrow C_0\delta_{R_0}(r)$  with

$$\delta_{R_0}(r) = \frac{1}{\pi\Gamma(3/4)R_0^3} \exp\left[-\left(\frac{r}{R_0}\right)^4\right], \quad (15)$$

where  $C_0$  is a constant and  $R_0 = 1.0$  fm determines the range of the regulator [21].

This potential corresponds to the smeared-out contact interaction which is used in the local chiral EFT interactions considered in Sec. IV C. Furthermore, up to

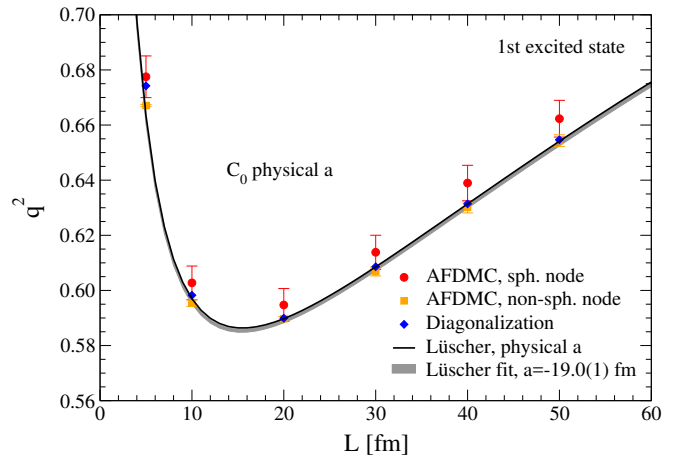


FIG. 2. (Color online) AFDMC results for the energy of two neutrons in the first excited state in finite volume with the potential (15) for different box sizes  $L$  (red circles) compared with the Lüscher formula (solid line). The error bars on the AFDMC results with a spherical nodal surface include both statistical uncertainties and a systematic uncertainty of 1% discussed in the text in Sec. IV B.  $C_0$  is adjusted to give the physical  $nn$  scattering length  $a = -18.9$  fm. The energies are given in terms of the dimensionless quantity  $q^2 = EML^2/(4\pi^2)$ . Also shown are the energies calculated by exact diagonalization (blue diamonds) as discussed in Sec. IV B.

the regulator, this potential corresponds to the interaction underlying the derivation of the Lüscher formula described in Sec. II. For our calculations we take  $L > R_0$  to minimize the finite-cutoff effects. Results obtained using this potential will serve as a benchmark for the AFDMC method in the two-particle system since we expect agreement with the Lüscher prediction up to statistical uncertainties.

Table I compares results of both the AFDMC and GFMC methods for representative box sizes. The GFMC calculations reproduce the AFDMC results within uncertainties, i.e., using the same number of configurations the uncertainties in the two methods are similar. Therefore, results will be shown only for the AFDMC method. Concerning the convergence of the sum in Eq. (14), we found for this potential that taking only the interaction in the original box into account is sufficient, which is consistent with the range of the potential.

Figure 1 compares the ground-state energies in terms of the dimensionless quantity  $q^2 = EML^2/(4\pi^2)$  obtained from AFDMC simulations with the exact solutions from the Lüscher formula for two different sets of scattering parameters. In the first case we used  $C_0 = -2.2369$  fm<sup>2</sup>, which corresponds to the physical value for the  $nn$  scattering length of  $a = -18.9$  fm and an effective range  $r_e = 1.096$  fm in infinite volume. The second case shows results for a potential with  $C_0 = -2.319$  fm<sup>2</sup> corresponding to a very large scattering length of  $a = -101.7$  fm and an effective range of  $r_e = 1.074$  fm. As can be seen, the agreement between

TABLE I. Comparison of ground-state results for two different potentials with both the AFDMC and GFMC methods for several box sizes  $L$ .

Potential	$L$ (fm)	$q^2$	
		AFDMC	GFMC
$C_0$ physical $a$	5	-0.1001(3)	-0.0999(1)
	10	-0.0879(7)	-0.0875(4)
	20	-0.069(2)	-0.072(2)
LO $R_0 = 1.0$ fm	5	-0.1179(6)	-0.1178(1)
	10	-0.0931(6)	-0.0940(4)
	20	-0.079(2)	-0.077(1)

the Lüscher results and the AFDMC simulations of the ground state is excellent over the full range of box sizes considered. It is worth pointing out the precision possible with the AFDMC method even at the extremely low densities of  $2/(50 \text{ fm})^3 \sim n_0/10^4$ , with  $n_0$  being the saturation density of nuclear matter.

In future applications, one could take finite-volume results from lattice QCD calculations, extract scattering parameters from them, and adjust LECs in chiral EFT interactions to match these scattering parameters. Here we demonstrate this idea by extracting the scattering parameters from the AFDMC results in several cases. We propagate the estimated uncertainties from the AFDMC simulations through the  $\chi^2$  fit discussed in Sec. II and fit the first two or three parameters of the effective range expansion. In particular, in order to see how robust the extraction of the infinite-volume scattering parameters from the AFDMC calculations is, we consider the contact potential with the very large scattering length. Here we performed a two-parameter fit to  $a$  and  $r_e$  by using the ground-state data yielding  $a = -98(4)$  fm and  $r_e = 1.066(7)$  fm which agree within the uncertainties with the infinite-volume parameters given above. Figure 1 shows the corresponding Lüscher result. The large uncertainty in the fitted scattering length of more than 4% could be reduced significantly when including more data at  $L \geq 20$  fm where  $a$  dominates the fit.

Results for excited-state energies of two neutrons with the contact potential with physical scattering length are shown in Fig. 2. AFDMC results are shown for both a spherical nodal surface as described in Sec. III and a nonspherical nodal surface, as will be introduced in Sec. IV B. The AFDMC results from the spherical node are systematically above the Lüscher results by  $\sim 1\%$ ; however, the overall trend is correctly reproduced. The global deviations can be understood when taking the assumption of a spherical nodal surface into account. An analysis of the systematic error related to this assumption will be discussed in the following section. The results from the nonspherical nodal surface reproduce the Lüscher results very accurately.

Figure 2 also shows a fit to the combined data of all AFDMC results for ground and excited states with the

improved nodal surface for the contact potential with physical scattering length. For the fit, the first three coefficients of the effective range expansion including the shape parameter were taken into account. The sensitivity to the shape parameter is largest for the states with largest momentum  $p$ , which correspond to excited states for small box sizes. As there are only a few of these contained in the data set the shape parameter cannot be determined with enough precision. The three-parameter fit yields a reduced  $\chi^2$  value of 0.74, a scattering length of  $a = -19.0(1)$  fm, and an effective range of  $r_e = 1.081(5)$  fm. These both agree well with the infinite-volume values given above. A more detailed discussion covering different aspects of extracting the scattering parameters from finite-volume energies of ground and excited states is given in Sec. IV C.

## B. Exact diagonalization and nodal surface

Diffusion Monte Carlo simulations do not provide direct access to the propagated wave function. To study the nodal structure of the wave function of two neutrons in a box we diagonalize the Hamiltonian in an appropriate basis. The computational effort can be minimized by choosing basis states satisfying the boundary conditions of the system under study. We are interested in the zero-total-momentum eigenstates of a cubic box with periodic boundary conditions. Furthermore, since we are limiting ourselves to  $S$ -wave states we only need to take basis functions of even parity into account. A convenient set of basis functions meeting these requirements is given by

$$\begin{aligned} \psi_{nmk}^{3D}(\mathbf{r}) &= \psi_n(x)\psi_m(y)\psi_k(z), \\ \psi_n(x) &= \sqrt{\frac{2 - \delta_{0n}}{L}} \cos\left(\frac{2\pi}{L}nx\right), \end{aligned} \quad (16)$$

where  $n = 0, 1, 2, \dots$  and  $\mathbf{r} = \mathbf{r}_1 - \mathbf{r}_2$ .

Exploiting further the cubic symmetry of the box, which implies that the eigenstates have to remain invariant under exchange of coordinates  $x, y, z$ , the number of basis states can be reduced by defining symmetrized states for  $n \leq m \leq k$ :

$$\begin{aligned} \psi_{nmk}^{3D \text{ sym}}(x, y, z) &= N \sum_{\{n, m, k\}} \psi_{nmk}^{3D}(x, y, z), \\ N &= \begin{cases} 1/\sqrt{6} & \text{for } n \neq m \neq k \\ 1/\sqrt{12} & \text{for } n = m \neq k \\ 1/6 & \text{for } n = m = k, \end{cases} \end{aligned} \quad (17)$$

where the sum runs over all permutations of  $\{n, m, k\}$ . The number of basis states implicitly set by  $n_{\max} > n, m, k$  has to be chosen such that the energy eigenstates are converged. As the box size  $L$  grows,  $n_{\max}$  has to be increased because higher momentum states contribute to the eigenstates. The calculations for  $L = 5, 10, 20, 30, 40, 50$  fm presented here were performed by using  $n_{\max} = 10, 16, 32, 48, 54, 54$ , respectively. Solving

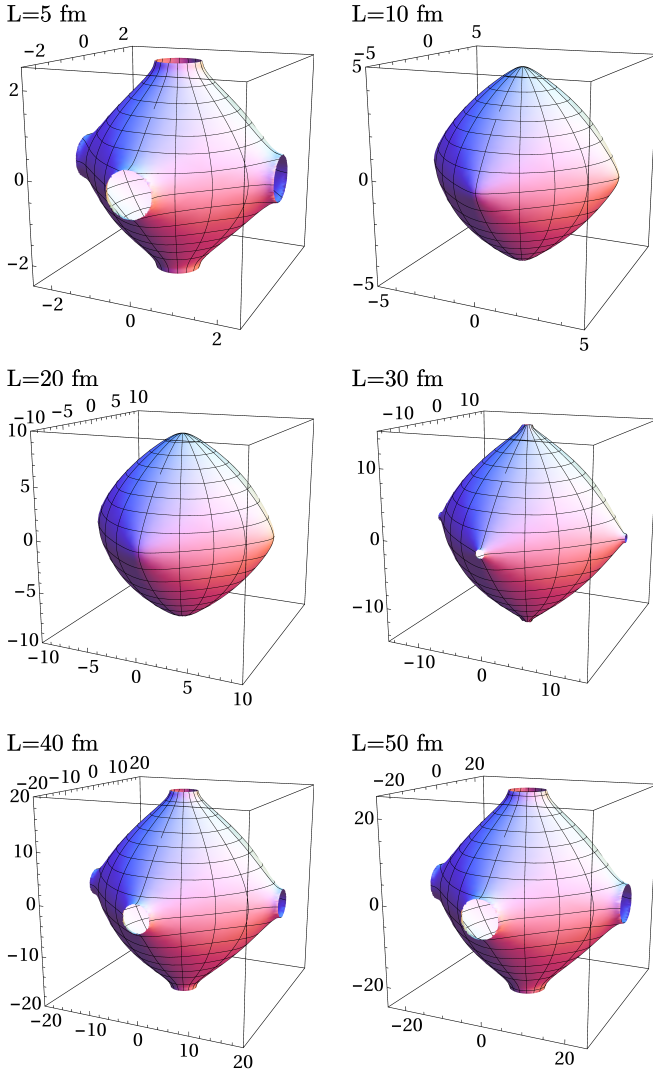


FIG. 3. (Color online) The nodal surfaces  $r_{\text{node}}(\theta, \phi)$  of the first excited states of the contact potential (15) with the physical  $nn$  scattering length  $a = -18.9$  fm for different box sizes  $L$ . The wave functions from which the nodal surfaces are extracted are obtained via diagonalization. See text for details.

the eigensystem  $H\psi = E\psi$  yields the eigenstates  $\psi_{\text{gs}}$  and  $\psi_{\text{ex}}$  corresponding to the ground- and first-excited-state energies  $E_0$  and  $E_1$  in terms of the basis defined in Eq. (17),

$$\psi_{\text{gs/ex}} = \sum_{\substack{n,m,k < n_{\text{max}} \\ n \leq m \leq k}} c_{nmk}^{\text{gs/ex}} \psi_{nmk}^{\text{3D sym}}. \quad (18)$$

The excited-state energies for the contact potential (15) with the physical  $nn$  scattering length  $a = -18.9$  fm are shown in Fig. 2. The results for the excited state from the diagonalization agree within 0.01% for  $L = 20, 30, 40$  fm with the exact results obtained from the Lüscher formula. At  $L = 5$  fm ( $L = 10$  fm) a deviation of 1.6% (0.2%) from the Lüscher result can be observed. For the small boxes, especially for  $L = 5$  fm, the range of the potential  $R_0$  and

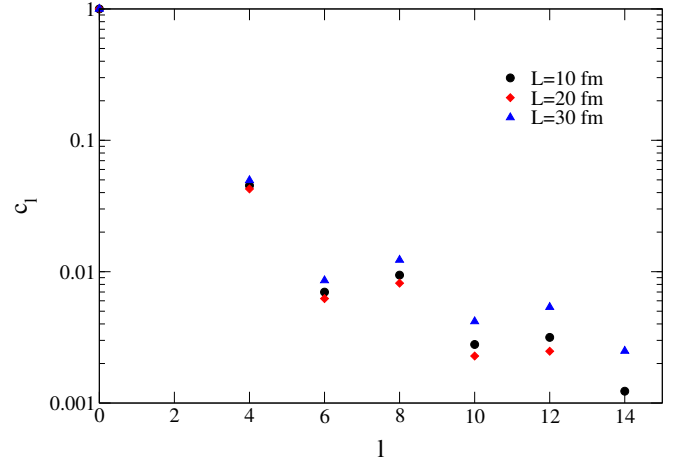


FIG. 4. (Color online) The coefficients  $c_l$  of the decomposition of the nodal surfaces in terms of cubic harmonics  $Y_l^c$  as in Eq. (21) as a function of  $l$ . The coefficients for each box size shown are normalized such that  $c_0 = 1$ . The  $y$ -axis is log scaled showing the power-law suppression of the two coefficients  $c_4$  and  $c_6$  with comparison to  $c_0$ .

the box size  $L$  are of the same order and the finite range of the contact potential (15) becomes relevant. Hence, a deviation from the Lüscher prediction is expected. For  $L = 50$  fm a deviation of  $\sim 0.1\%$  was obtained implying that  $n_{\text{max}}$  needs to be increased in order to reach convergence.

The nodal surface  $r_{\text{node}}(\theta, \phi)$  can be extracted from the wave function of the excited state by solving  $\psi_{\text{ex}}(r_{\text{node}}, \theta, \phi) = 0$  for  $\theta \in [0, \pi]$ ,  $\phi \in [0, 2\pi]$ . Figure 3 shows the nodal surfaces for different box sizes. For the contact potential (15) with the physical  $nn$  scattering length  $a = -18.9$  fm, the nodal surface is not spherical for any box size and not even closed for box sizes of 5, 30, 40, and 50 fm. To estimate the systematic error caused by assuming spherical symmetry in the nodal surface for the AFDMC simulations, we decomposed the nodal surfaces in real spherical harmonics  $Y_{lm}$ :

$$r_{\text{node}}(\theta, \phi) = \sum_{l=0}^{\infty} \sum_{m=-l}^l c_{lm} Y_{lm}(\theta, \phi). \quad (19)$$

We found that the coefficients  $c_{lm}$  vanish for all  $l, m$  other than  $l = 0, 4, 6, 8, \dots$  and  $m = 0, 4, 8, \dots$ , which suggests that there is a more appropriate set of functions in which one can expand the nodal surface. Indeed, in a cubic box the rotation symmetry group is broken down to the cubic symmetry group  $O_h$ . The irreducible representation of  $O_h$  is given by combinations of spherical harmonics, so-called cubic harmonics  $Y_l^c$ , with

$$Y_l^c(\theta, \phi) = \sum_{m=0,4,8,\dots} a_{lm} Y_{lm}(\theta, \phi), \quad (20)$$

where the coefficients  $a_{lm}$  are given in Ref. [38]. We found that for a given  $l$  the coefficients  $c_l = \frac{c_{lm}}{a_{lm}}$  agree for all

$|m| \leq l$ . Hence, as expected it is possible to expand the nodal surface in terms of cubic harmonics,

$$r_{\text{node}}(\theta, \phi) = \sum_l c_l Y_l^c(\theta, \phi). \quad (21)$$

The corresponding coefficients  $c_l$  for box sizes where the nodal surface is closed ( $L = 10, 20$  fm) and almost closed ( $L = 30$  fm) are shown in Fig. 4. Note that the coefficients are normalized such that  $c_0 = 1$ .  $c_0$  being much larger than  $c_l$  for  $l \geq 4$  justifies the approximation of the nodal surface as a sphere used in the AFDMC simulations because the spherical contribution from  $Y_0^c$  dominates the nodal surface. We do not perform the decomposition for the other box sizes since the holes in the surfaces cause large uncertainties when decomposing into cubic harmonics.

The radial solution of the two-particle scattering problem in infinite volume can be written in terms of spherical Bessel functions  $j_l(pr)$ . For  $pr \ll 1$ , the Bessel functions behave as  $j_l(pr) \sim (pr)^l$ . In a cubic box the lowest-possible momentum is  $p \sim 1/L$ . As the excited states are completely determined by the nodal surface, which in our case is described by its radius  $r_{\text{node}}$ , naive dimensional analysis suggests that we can identify  $r = r_{\text{node}}$ . Hence, we expect that higher- $l$  contributions are suppressed by  $(r_{\text{node}}/L)^l$  when comparing to the leading contribution. Indeed, the coefficients  $c_4$  and  $c_6$ , shown in Fig. 4, are suppressed according to a power law compared with the leading spherical contribution with  $l = 0$ .

Although this is no longer true for  $l > 6$ , the argument can still serve as an estimate of the systematic uncertainty introduced through the assumption of a spherical nodal surface in the AFDMC simulations of the first excited state. A perturbative expansion of the energy in terms of different  $l$  contributions to the wave function,

$$E = \langle \psi_{l=0} | H | \psi_{l=0} \rangle + c_4^2 \langle \psi_{l=4} | H | \psi_{l=4} \rangle + \dots, \quad (22)$$

implies a correction proportional to  $(c_4)^2$  when assuming that  $\langle \psi_l | H | \psi_l \rangle$  is of the same order for all  $l$ . Taking into account that the suppression seems to decrease with higher  $l$  we estimate  $(c_4)^2$  conservatively as being of the order of 1% even though  $c_4 \approx 0.045$  (see Fig. 4). Therefore, an additional systematic error of 1% is added to the statistical uncertainties from the QMC simulations in Figs. 2 and 7.

Furthermore, it is clear that the nodal surfaces shown in Fig. 3 are less spherical for box sizes where the surface is not closed. This statement is supported by Fig. 4 where the coefficients for  $L = 30$  fm are larger than the other contributions. This matches the deviations of AFDMC results with the spherical node from the Lüscher predictions in Figs. 2 and 7, which are largest for  $L = 5, 40, 50$  fm.

Our diagonalization study suggests that a large improvement in our AFDMC results can be obtained by incorporating the first nonspherical contribution into the nodal surface

$$r_{\text{node}}(\theta, \phi) = c_0 Y_0^c(\theta, \phi) + c_4 Y_4^c(\theta, \phi). \quad (23)$$

As discussed in Sec. III separate QMC runs were performed on the two sides of the nodal surface in order to find an optimal set of parameters  $c_0$  and  $c_4$ . Details on how the nonspherical nodal surface was incorporated into the Jastrow wave function can be found in Appendix B.

As can be seen in Fig. 2, the improved nodal surface yields AFDMC results much closer to the Lüscher prediction. However, one can see still some disagreement between the three methods employed (diagonalization, AFDMC, and Lüscher) at the smallest box size considered,  $L = 5$  fm. The results coming from the exact diagonalization and the AFDMC results should agree well, as they do for larger box sizes. That they do not suggests that our improved nodal surface is likely missing higher-order  $Y_l^c$  contributions and the associated uncertainties might be underestimated. Since the Lüscher results are based on the effective range expansion, while the diagonalization uses the full potential, deviations at large energies (corresponding to small box sizes) are expected as soon as the effective range expansion is no longer accurate enough to describe the phase shift.

### C. Chiral EFT interactions

In this section, we present results for the different local chiral EFT potentials from Ref. [21]. To avoid large statistical uncertainties, QMC simulations require interactions where all momentum dependencies up to quadratic terms can be separated. This requirement is met by local potentials [18]. However, chiral EFT interactions are usually formulated in momentum space and are typically nonlocal. Local chiral  $NN$  potentials have been developed recently up to next-to-next-to-leading order (N<sup>2</sup>LO) in the chiral power counting and applied in calculations of neutron matter, light nuclei, and neutron-alpha scattering using continuum QMC methods [20–24].

Table I compares results for the leading chiral potential for both GFMC and AFDMC methods. As discussed before, uncertainty estimates are very similar and we limit our plots to results from the AFDMC method.

The range of the chiral potentials exceeds the range of the contact potential in Eq. (15). A check for convergence shows that, for box sizes up to  $L = 20$  fm, inclusion of copies of the original box up to the second-to-nearest is required to reach truncation uncertainties comparable to the statistical errors, while beyond  $L = 20$  fm at most the nearest copies need to be included.

In Fig. 5 we show results of AFDMC simulations which were performed using the chiral leading-order (LO) potential for  $R_0 = 1.0$  fm and  $R_0 = 1.2$  fm, corresponding to cutoffs of 500 MeV and 400 MeV in momentum space, respectively. The corresponding scattering lengths and effective ranges were obtained by calculating phase shifts in the infinite volume. Similar to the previous cases we compare Lüscher results by using the scattering parameters to AFDMC results for different box sizes. Figure 6 shows results for the chiral NLO and N<sup>2</sup>LO potentials for

$R_0 = 1.0$  fm. In all cases the overall agreement for box sizes  $L \geq 10$  fm is excellent, while the AFDMC results for ground-state energies at  $L = 5$  fm start to deviate from the Lüscher prediction. In Fig. 7 results for the excited states of the chiral LO potential for both a spherical nodal surface as described in Sec. III and a nonspherical nodal surface as introduced in Sec. IV B are shown. While the spherical node over-predicts at large  $L$ , the improved nodal surface yields results consistent with the Lüscher prediction in this region. However, in this context it is worth pointing out that for the chiral potentials the nodal surfaces tend to be more deformed than for the contact potential, which implies that the uncertainties for the small boxes are likely underestimated.

As discussed in Sec. II the analytic continuation of the Lüscher formula is limited to the threshold of pionless EFT  $|p| < m_\pi/2$ . Figures 5 – 7 show the corresponding maximal value for  $q^2$ . The absolute values of the AFDMC energies for  $L = 5$  fm (ground states) and  $L = 5, 10$  fm (excited state) for the different chiral potentials exceed the threshold of pionless EFT, and hence the (exponentially suppressed) disagreement is to be expected. In the end, this effect reflects the necessity of including pions in the effective theory for the correct description of processes where momenta are of the order of the pion mass. However, we find that the size of the corrections is smaller than naively expected: for the smallest box size with  $m_\pi L = 3.5$  the leading effect should scale as  $c_1 e^{-m_\pi L} = 18\%$  [34], where  $c_1 = 6$  denotes the multiplicity of nearest neighbors, but the actually observed deviation merely amounts to about 3%. This finding could be related to the observation in [34] that, for a realistic  $NN$  potential, the effective scale in the exponent can exceed the pion mass, leading to a stronger suppression than expected from the one-pion exchange alone.

Figure 8 shows phase shifts obtained by solving Eq. (1) for the AFDMC results for the excited state with the LO chiral potential shown in Fig. 7 (red circles and orange squares). A direct extraction of phase shifts from finite-volume energies is only possible for states with  $E > 0$  as only the effective-range expansion provides an analytic continuation to imaginary momenta corresponding to bound states. We compare the AFDMC results to the phase shifts obtained by solving the  $nn$  scattering problem for the same chiral LO potential in infinite volume (black line). As in Fig. 7, the overall trend is correctly reproduced by both spherical and nonspherical node results. We show again in gray the region for which momenta exceed the regime of pionless EFT,  $|p| > m_\pi/2$ . The AFDMC data with a spherical node underestimate the phase shift over the whole region. The improved nodal surface yields phase shifts in very good agreement with the infinite-volume phase shift at small momenta. Beyond the regime of pionless EFT the results are still too low but are significantly closer to the phase shift than the spherical node results. We also show the phase shift obtained from the effective range expansion with the first two parameters  $a = -18.9$  fm and  $r_e = 2.01$  fm (dashed

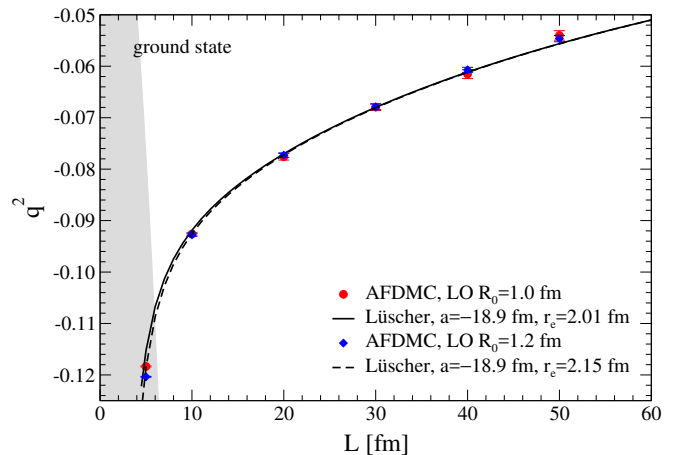


FIG. 5. (Color online) AFDMC results for the energy of two neutrons in the ground state in finite volume with the LO chiral EFT interaction compared with the Lüscher formula for different box sizes  $L$ . The cutoffs  $R_0 = 1.0$  fm (red circles and solid line) and  $R_0 = 1.2$  fm (blue diamonds and dashed line) are used. The energies are given in terms of the dimensionless quantity  $q^2 = EML^2/(4\pi^2)$ . The region where  $|p| > m_\pi/2$  is indicated by the gray band; see Sec. II.

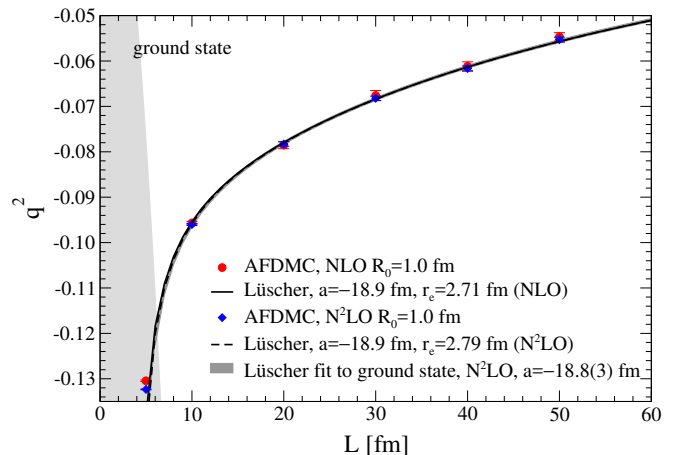


FIG. 6. (Color online) AFDMC results for the energy of two neutrons in the ground state in finite volume with the NLO and  $N^2$ LO chiral EFT interactions with cutoff  $R_0 = 1.0$  fm compared with the Lüscher formula for different box sizes  $L$ . The results at NLO ( $N^2$ LO) are given as the red circles and solid line (blue diamonds and dashed line). The dark gray band shows a fit (as described in the text) to the AFDMC results for the  $N^2$ LO chiral potential. The energies are given in terms of the dimensionless quantity  $q^2 = EML^2/(4\pi^2)$ . Points in the region  $|p| > m_\pi/2$  indicated by the gray band are not included in the fit; see Sec. II.

line), as used for the Lüscher result in Fig. 7. For momenta above the strict range of validity, the AFDMC results are larger than the phase shift from the truncated effective range expansion. This corresponds to Fig. 7 where these points lie below the Lüscher result.

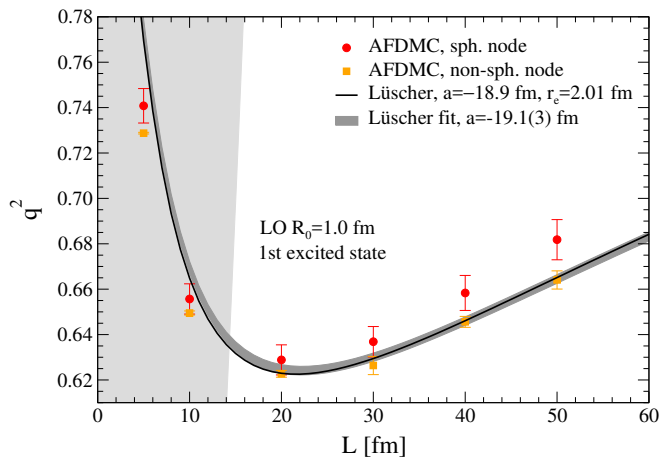


FIG. 7. (Color online) AFDMC results for the energy of two neutrons in the first excited state in finite volume with the LO chiral EFT interaction with cutoff  $R_0 = 1.0$  fm (red circles) compared with the Lüscher formula (solid line) for different box sizes  $L$ . The error bars on the AFDMC results with a spherical nodal surface include both statistical uncertainties and a systematic uncertainty of 1 % discussed in the text in Sec. IV B. The dark gray band shows a combined fit (as described in the text) to the ground- and first-excited-state AFDMC results for the LO chiral potential. The energies are given in terms of the dimensionless quantity  $q^2 = EML^2/(4\pi^2)$ . Points in the region  $|p| > m_\pi/2$  indicated by the gray band are not included in the fit; see Sec. II.

## V. CONCLUSIONS

In this work, we present first results for the two-neutron finite-volume ground and first-excited states using AFDMC, both for a contact potential and chiral EFT interactions. To extract the excited-state energy we used an approximate method based on an iterative determination of the nodal surface of the excited-state wave function, with systematic uncertainties estimated by direct diagonalization of the contact-potential Hamiltonian. Having obtained the exact nodal surfaces through the diagonalization, we incorporated nonspherical nodal surfaces in the AFDMC method, which significantly improves results for the excited states. Using Lüscher's method to extract the scattering length and effective range from fits to the finite-volume energy levels of the ground and excited state, we found good agreement with the scattering parameters determined directly in infinite volume, which demonstrates the viability of the AFDMC approach for the calculation of the finite-volume two-particle spectrum.

In this way, our work establishes QMC techniques as powerful methods for the matching of chiral EFT and lattice QCD results. By equating the finite-volume energy levels one can directly determine the LECs in the chiral potential without the necessity of first extracting the infinite-volume phase shift. Advantages of this procedure concern the fact that it evades limitations of the Lüscher

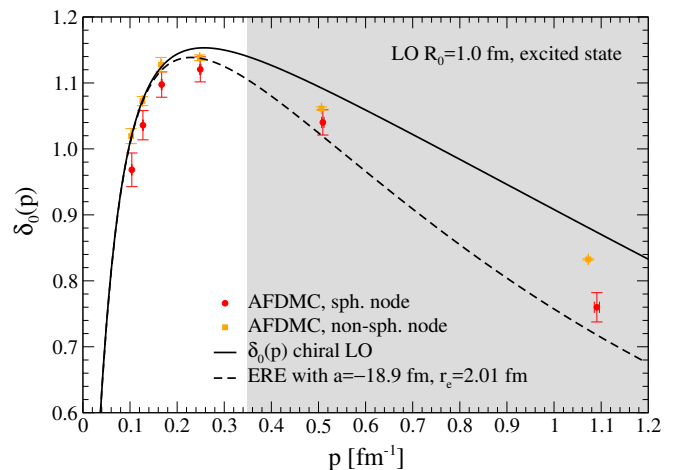


FIG. 8. (Color online)  $^1S_0$   $nn$  phase shift  $\delta_0(p)$  from AFDMC results for the first excited state in finite volume with the LO chiral EFT interaction with cutoff  $R_0 = 1.0$  fm with spherical nodal surface (red circles) and nonspherical nodal surface (orange squares) compared with the phase shift obtained from  $nn$  scattering in infinite volume (solid line). The error bars on the AFDMC results include both statistical uncertainties and a systematic uncertainty of 1 % discussed in the text in Sec. IV B. The dashed line shows the phase shift obtained from the effective range expansion (ERE) with  $a = -18.9$  fm and  $r_e = 2.01$  fm. The region where  $|p| > m_\pi/2$  is indicated by the gray band; see Sec. II.

formula for small volumes and should generalize straightforwardly to the multi-body system, to avoid the complexity typically inherent in the extension of Lüscher's approach beyond the two-body sector. For the extraction of resonance properties along these lines, we anticipate control over excited states to be essential. In this regard, the recovery of the virtual state in the two-neutron system as reflected by the large scattering length, both in the ground and first excited state, can be considered a successful proof of principle.

## ACKNOWLEDGMENTS

We thank J. A. Carlson, Z. Davoudi, A. Rusetsky, M. J. Savage, K. E. Schmidt, S. R. Sharpe, and K. A. Wendt for helpful discussions. This work was supported in part by the ERC Grant No. 307986 STRONGINT, the Deutsche Forschungsgemeinschaft through Grant SFB 1245, the US Department of Energy Grant Nos. DE-AC52-06NA25396 and DE-FG02-00ER41132, the National Science Foundation Grant No. PHY-1430152 (JINA-CEE), the NUCLEI SciDAC program, the LANL LDRD program, and the Natural Sciences and Engineering Research Council of Canada. The computations were performed at the Jülich Supercomputing Center as well as at NERSC, which is supported by the US Department of Energy Contract No. DE-AC02-05CH11231. We thank the Institute for Nuclear Theory at the University

of Washington for its hospitality and the Department of Energy for partial support during the completion of this work.

### Appendix A: Evaluation of $S(\eta)$

The definition of  $S(\eta)$  that appears in Eq. (2) can be evaluated numerically; however, in practice it converges relatively slowly. A more efficient approach used in Ref. [2] relies on Poisson's summation formula as well as the fact that  $S(\eta)$  equals the analytic continuation of

$$Z_{00}(s, \eta) = \sum_{\mathbf{j}} \frac{1}{(\mathbf{j}^2 - \eta)^s}, \quad \text{Re } s > \frac{3}{2}, \quad (\text{A1})$$

for  $s \rightarrow 1$ , which leads to

$$S(\eta) = \sum_{\mathbf{j}^2 < \eta} \frac{1}{\mathbf{j}^2 - \eta} + \int_0^1 dt F_{00}^1(t, \eta) + \int_1^\infty dt F_{00}(t, \eta) + \sum_{i=0}^1 \left( \frac{A_i}{i+1} + \frac{B_i}{i-\frac{1}{2}} \right), \quad (\text{A2})$$

where

$$\begin{aligned} F_{00}^1(t, \eta) &= - \sum_{\mathbf{j}^2 \leq \eta} e^{t(\eta - \mathbf{j}^2)} + \left( \frac{\pi}{t} \right)^{3/2} e^{t\eta} \sum_{\mathbf{j}} e^{-\frac{\pi^2}{t} \mathbf{j}^2} \\ &\quad - \sum_{i=0}^1 (A_i t^i + B_i t^{i-3/2}), \\ F_{00}(t, \eta) &= \sum_{\mathbf{j}^2 > \eta} e^{-t(\mathbf{j}^2 - \eta)}, \\ A_i &= - \frac{1}{i!} \sum_{\mathbf{j}^2 \leq \eta} (\eta - \mathbf{j}^2)^i, \\ B_i &= \pi^{3/2} \frac{\eta^i}{i!}. \end{aligned} \quad (\text{A3})$$

This representation accelerates convergence exponentially and can be easily implemented by using standard integration routines.

### Appendix B: Jastrow wave function for nonspherical nodal surfaces

The Jastrow wave function  $\psi_J(r)$  commonly used in QMC simulations is given by the solutions of the radial Schrödinger equation with the central part of the potential. The solutions are required to meet the following boundary conditions:

$$\begin{aligned} \psi_J(0) &= u_0, \\ \psi_J(L/2) &= 1, \\ \psi_J'(0) &= 0, \\ \psi_J'(L/2) &= 0, \end{aligned} \quad (\text{B1})$$

where  $u_0$  is a constant. Furthermore, for the ground-state trial wave function it is required that there be no nodes in  $\psi_J(r)$ .

The spherical nodal surface was implemented by constructing a Jastrow function with a single node. This was achieved by writing the Jastrow in terms of a sum of different solutions of the radial Schrödinger equation

$$\psi_J^{\text{sph}}(r) = N(\psi_J^1(r) - c \psi_J^0(r)), \quad (\text{B2})$$

where  $N$  denotes a normalization constant and the superscript in  $\psi_J^i(r)$  denotes the number of nodes. By changing the parameter  $c$  it is possible to adjust the position  $r_{\text{node}}$  of the node such that  $\psi_J^{\text{sph}}(r_{\text{node}}) = 0$ .

To improve the nodal surface in the QMC method we take advantage of the analysis of the nodal surface obtained from the diagonalization in Sec. IV B. Usually the Jastrow function is a radial function only allowing for spherical nodal surfaces. If the nonspherical nodal surface is to be reproduced by the Jastrow function, angular dependencies have to be introduced.

Including the first nonspherical contribution in the nodal surface corresponds to adding the cubic harmonic with  $l = 4$  to the spherical term:

$$r_{\text{node}}(\hat{\mathbf{r}}) = c_0 Y_0^c(\hat{\mathbf{r}}) + c_4 Y_4^c(\hat{\mathbf{r}}), \quad (\text{B3})$$

where  $Y_l^c$  denote cubical harmonics and  $\hat{\mathbf{r}} = \mathbf{r}/r$  is the unit vector pointing in the direction of  $\mathbf{r}$ .  $c_0$  and  $c_4$  are coefficients defining the nodal surface.

The function defined by

$$f_{\text{non-sph}}(\mathbf{r}) = \psi_J^1(r) - \frac{\psi_J^1(r_{\text{node}}(\hat{\mathbf{r}}))}{\psi_J^0(r_{\text{node}}(\hat{\mathbf{r}}))} \psi_J^0(r) \quad (\text{B4})$$

vanishes when  $r = r_{\text{node}}$  for a given direction  $\hat{\mathbf{r}}$ . However, this function does not meet the boundary conditions in Eq. (B1). Furthermore it is not continuous at  $r \rightarrow 0$  since for vectors  $\mathbf{r}_1$  and  $\mathbf{r}_2$  pointing in different directions

$$\lim_{r_1 \rightarrow 0} f_{\text{non-sph}}(\mathbf{r}_1) \neq \lim_{r_2 \rightarrow 0} f_{\text{non-sph}}(\mathbf{r}_2). \quad (\text{B5})$$

Therefore, the function defined in Eq. (B4) is multiplied by a normalizing function

$$\begin{aligned} n(\mathbf{r}) &= n_3(\hat{\mathbf{r}})r^3 + n_2(\hat{\mathbf{r}})r^2 + n_1(\hat{\mathbf{r}})r + n_0(\hat{\mathbf{r}}), \\ n_3(\hat{\mathbf{r}}) &= \frac{16}{L^3} \left( \frac{u_0}{a(\hat{\mathbf{r}})} - \frac{1}{b(\hat{\mathbf{r}})} \right), \\ n_2(\hat{\mathbf{r}}) &= \frac{12}{L^2} \left( \frac{1}{b(\hat{\mathbf{r}})} - \frac{u_0}{a(\hat{\mathbf{r}})} \right), \\ n_1(\hat{\mathbf{r}}) &= 0, \\ n_0(\hat{\mathbf{r}}) &= \frac{u_0}{a(\hat{\mathbf{r}})}, \end{aligned} \quad (\text{B6})$$

where

$$\begin{aligned} a(\hat{\mathbf{r}}) &= f_{\text{non-sph}}(\mathbf{r})|_{r=0}, \\ b(\hat{\mathbf{r}}) &= f_{\text{non-sph}}(\mathbf{r})|_{r=L/2}, \end{aligned} \quad (\text{B7})$$

and  $u_0 < 0$  defines the value of the Jastrow at  $r = 0$ . The nonspherical Jastrow is then given by

$$\psi_J^{\text{non-sph}}(\mathbf{r}) = f_{\text{non-sph}}(\mathbf{r})n(\hat{\mathbf{r}}), \quad (\text{B8})$$

which obeys the required conditions in Eq. (B1). Now, the excited-state energies can be found as discussed in Sec. III by adjusting the parameters  $c_0$  and  $c_4$ .

- 
- [1] S. R. Beane, W. Detmold, K. Orginos, and M. J. Savage, *Prog. Part. Nucl. Phys.* **66**, 1 (2011).
- [2] M. Lüscher, *Commun. Math. Phys.* **105**, 153 (1986).
- [3] M. Lüscher, *Nucl. Phys. B* **354**, 531 (1991).
- [4] S. Kreuzer and H.-W. Hammer, *Phys. Lett. B* **694**, 424 (2011).
- [5] K. Polejaeva and A. Rusetsky, *Eur. Phys. J. A* **48**, 67 (2012).
- [6] R. A. Briceño and Z. Davoudi, *Phys. Rev. D* **87**, 094507 (2013).
- [7] M. T. Hansen and S. R. Sharpe, *Phys. Rev. D* **92**, 114509 (2015).
- [8] S. R. Beane, P. F. Bedaque, A. Parreño, and M. J. Savage, *Phys. Lett. B* **585**, 106 (2004).
- [9] S. Weinberg, *Phys. Lett. B* **251**, 288 (1990).
- [10] S. Weinberg, *Nucl. Phys. B* **363**, 3 (1991).
- [11] P. F. Bedaque and U. van Kolck, *Annu. Rev. Nucl. Part. Sci.* **52**, 339 (2002).
- [12] E. Epelbaum, H.-W. Hammer, and U.-G. Meißner, *Rev. Mod. Phys.* **81**, 1773 (2009).
- [13] R. Machleidt and D. R. Entem, *Phys. Rept.* **503**, 1 (2011).
- [14] H.-W. Hammer, A. Nogga, and A. Schwenk, *Rev. Mod. Phys.* **85**, 197 (2013).
- [15] J. W. Holt, N. Kaiser, and W. Weise, *Prog. Part. Nucl. Phys.* **73**, 35 (2013).
- [16] K. Hebeler, J. D. Holt, J. Menéndez, and A. Schwenk, *Annu. Rev. Nucl. Part. Sci.* **65**, 457 (2015).
- [17] A. Gardestig, *J. Phys. G* **36**, 053001 (2009).
- [18] J. Carlson, S. Gandolfi, F. Pederiva, S. C. Pieper, R. Schiavilla, K. E. Schmidt, and R. B. Wiringa, *Rev. Mod. Phys.* **87**, 1067 (2015).
- [19] S. Gandolfi, A. Gezerlis, and J. Carlson, *Annu. Rev. Nucl. Part. Sci.* **65**, 303 (2015).
- [20] A. Gezerlis, I. Tews, E. Epelbaum, S. Gandolfi, K. Hebeler, A. Nogga, and A. Schwenk, *Phys. Rev. Lett.* **111**, 032501 (2013).
- [21] A. Gezerlis, I. Tews, E. Epelbaum, M. Freunek, S. Gandolfi, K. Hebeler, A. Nogga, and A. Schwenk, *Phys. Rev. C* **90**, 054323 (2014).
- [22] J. E. Lynn, J. Carlson, E. Epelbaum, S. Gandolfi, A. Gezerlis, and A. Schwenk, *Phys. Rev. Lett.* **113**, 192501 (2014).
- [23] I. Tews, S. Gandolfi, A. Gezerlis, and A. Schwenk, *Phys. Rev. C* **93**, 024305 (2016).
- [24] J. E. Lynn, I. Tews, J. Carlson, S. Gandolfi, A. Gezerlis, K. E. Schmidt, and A. Schwenk, *Phys. Rev. Lett.* **116**, 062501 (2016).
- [25] N. Barnea, L. Contessi, D. Gazit, F. Pederiva, and U. van Kolck, *Phys. Rev. Lett.* **114**, 052501 (2015).
- [26] J. Kirscher, N. Barnea, D. Gazit, F. Pederiva, and U. van Kolck, *Phys. Rev.* **C92**, 054002 (2015).
- [27] M. Lüscher, *Nucl. Phys. B* **364**, 237 (1991).
- [28] V. Bernard, U.-G. Meißner, and A. Rusetsky, *Nucl. Phys. B* **788**, 1 (2008).
- [29] W. M. C. Foulkes, L. Mitas, R. J. Needs, and G. Rajagopal, *Rev. Mod. Phys.* **73**, 33 (2001).
- [30] S. C. Pieper, R. B. Wiringa, and J. Carlson, *Phys. Rev. C* **70**, 054325 (2004).
- [31] D. B. Kaplan, M. J. Savage, and M. B. Wise, *Nucl. Phys. B* **534**, 329 (1998).
- [32] U. van Kolck, *Nucl. Phys. A* **645**, 273 (1999).
- [33] J.-W. Chen, G. Rupak, and M. J. Savage, *Nucl. Phys. A* **653**, 386 (1999).
- [34] I. Sato and P. F. Bedaque, *Phys. Rev. D* **76**, 034502 (2007).
- [35] S. Gandolfi, A. Lovato, J. Carlson, and K. E. Schmidt, *Phys. Rev. C* **90**, 061306 (2014).
- [36] B. S. Pudliner, V. R. Pandharipande, J. Carlson, and R. B. Wiringa, *Phys. Rev. Lett.* **74**, 4396 (1995).
- [37] S. Zhang and H. Krakauer, *Phys. Rev. Lett.* **90**, 136401 (2003).
- [38] J. Muggli, *J. appl. Math. Phys. (ZAMP)* **23**, 311 (1972).